

Efficient, Interpretable Atomistic Graph Neural Network Representation for Angle-dependent Properties and its Application to Optical Spectroscopy Prediction

Tim Hsu^{*1}, Nathan Keilbart², Stephen Weitzner², James Chapman², Penghao Xiao³, Tuan Anh Pham², S. Roger Qiu², Xiao Chen¹, and Brandon C. Wood²

¹Center for Applied Scientific Computing, Lawrence Livermore National Laboratory, Livermore, CA, USA

²Materials Science Division, Lawrence Livermore National Laboratory, Livermore, CA, USA

³Department of Physics and Atmospheric Science, Dalhousie University, Halifax, NS, Canada

September 27, 2021

Abstract

Graph neural networks (GNNs) are attractive for learning properties of atomic structures thanks to their intuitive, physically informed graph encoding of atoms and bonds. However, conventional GNN encodings do not account for angular information, which is critical for describing complex atomic arrangements in disordered materials, interfaces, and molecular distortions. In this work, we extend the recently proposed ALIGNN encoding, which incorporates bond angles, to also include dihedral angles (ALIGNN-d), and we apply the model to capture the structures of aqua copper complexes for spectroscopy prediction. This simple extension is shown to lead to a memory-efficient graph representation capable of capturing the full geometric information of atomic structures. Specifically, the ALIGNN-d encoding is a sparse yet equally expressive representation compared to the dense, maximally-connected graph, in which all bonds are encoded. We also explore model interpretability based on ALIGNN-d by elucidating the relative contributions of individual structural components to the optical response of the copper complexes. Lastly, we briefly discuss future developments to validate the computational efficiency and to extend the interpretability of ALIGNN-d.

1 Introduction

In materials science, graph neural networks (GNNs) have been popular as a surrogate model for learning properties of materials and molecular systems [1–6]. This popularity is partly due to the intuitive, physically-informed graph representation or encoding that represents atoms with nodes and bonds with edges. Beyond atom and bond features, encoding further structural information can be helpful or even required for certain property prediction tasks. For example, the bond angle is a critical feature for properties associated with electronic structure and bond hybridization [7–10], especially in disordered systems where slight perturbations in geometry can greatly impact resulting properties. However, typical GNNs for atomic systems do not encode angular information and therefore may not effectively learn to predict angle- or geometry-sensitive properties.

To address this challenge, several approaches have been proposed to explicitly encode bond angles [11, 12], or directional information such that bond angles can be implicitly retrieved [13, 14]. DimeNet [11] and paiNN [13] were designed for non-periodic molecular structures. ALIGNN [12], which explicitly represents bond angles with (edges of) line graphs, is a general formulation applicable to non-periodic molecular graphs, as well as crystal graphs that represent periodic/crystalline

^{*}Corresponding Author, hsu16@llnl.gov

systems [4, 15]. However, such encoding is still not guaranteed to capture a system’s full structural information. Further, despite the line graph’s intended purpose for explicitly capturing angles, the authors of ALIGNN did not specifically test the expressive power of such representation for learning geometry-sensitive properties.

Therefore, in this work, we expanded the ALIGNN encoding in order to capture a system’s full structural information, and investigated the expressive power of such representation for spectroscopy prediction of disordered/distorted aqua copper complexes, which are copper ions coordinated by water molecules. This enhanced graph representation, named ALIGNN-d (d for dihedral), is a generalization of ALIGNN, in which the line graph construction is based on bond angles formed by pairs of adjacent bonds. However, more generally, angles associated with any pairs of bonds, adjacent or otherwise, may also be encoded into the line graph. We determined the necessary angular information to encode by following the principle of the Z-matrix [16], which represents molecular structures in terms of sequences of atomic numbers, bond lengths, bond angles, and dihedral angles. Importantly, the Z-matrix can be converted back to the Cartesian space, in terms of the spatial coordinates of the atoms. Therefore, extended from ALIGNN, ALIGNN-d additionally includes dihedral angle information and in principle is capable of fully describing an atomic system’s complete structure.

To empirically prove the expressive power of ALIGNN-d, we trained GNN models based on different graph representations, with and without line graphs, to predict spectral signatures of aqua copper complexes, a geometry-sensitive property. Based on the results, a minimally-connected graph akin to typical molecular graph representations, combined with the corresponding line graph (with dihedral angles), leads to roughly the same predictive accuracy as that based on the maximally-connected graph, in which all pairwise bonds are encoded, but with significantly fewer edges (31–35%). In addition, the loss convergence based on the ALIGNN and ALIGNN-d encodings, i.e., representations with auxiliary line graphs, is faster and more stable than those without line graphs. We also demonstrate a unique opportunity for exploring model interpretability enabled by the explicit graph representation of bond angles and dihedral angles. Specifically, based on an “interpretable” training design, graph components representing angles are shown to have generally greater contributions to model prediction than those representing atoms and bonds.

In summary, our main contributions are as follows. First, we extended the original ALIGNN graph representation to also encode dihedral angles. Such implementation leads to a principled, memory-efficient approach to graph encoding, requiring only a minimally-connected graph and its corresponding line graph to capture the full structural information of atomic systems. Second, we trained GNN models with line graphs to specifically learn angle-dependent properties in disordered systems. This application further reveals the capabilities of line graphs, as ALIGNN has only been recently introduced for general material property prediction. Lastly, as the first work in atomistic modeling to explore model interpretability for GNNs with auxiliary line graphs, we visualized relative contributions of all graph components (atoms, bonds, and angles) to prediction output in an intuitive graph format. This exploration sheds light on the merit of constructing more elaborate graph representations to better capture atomic structures.

2 Methods

This section describes the methods for data preparation; data processing and analysis; graph representations; model formulation; and model training. During data preparation, structures of aqua copper complexes were sampled from molecular dynamics simulations, and their spectral signatures were calculated using time-dependent density functional theory simulations. We processed the spectral data in order to simplify the output format for training a structure-to-spectrum GNN model. Based on a brief analysis using Continuous Shape Measure, we confirmed that the spectral signatures are indeed sensitive to geometry. Finally, we built GNN models based on different graph representations, with and without line graphs, and trained them to predict spectral signatures.

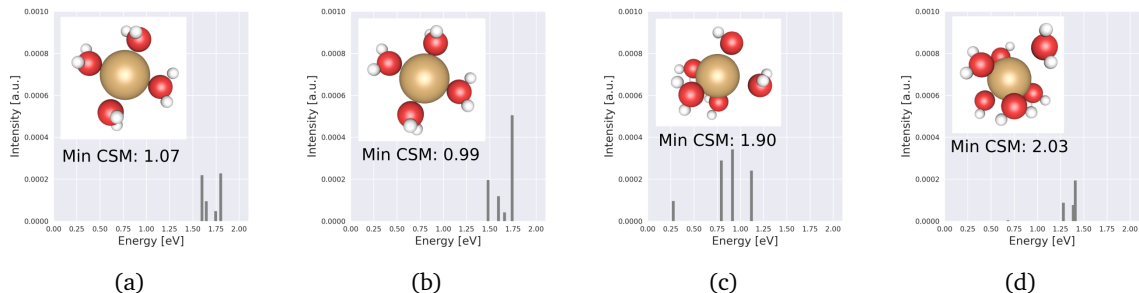


Figure 1: Each structural configuration of the aqua complex (figure insets) corresponds to a spectral signature (vertical discrete lines). Slight structural perturbations (a, b) result in noticeably different shifts of the overall peak locations (x-axis) and intensities (y-axis). In our dataset, the central copper ion (colored in orange) is surrounded by either 4 (a, b), 5 (c), or 6 (d) water molecules (oxygen in red, hydrogen in white). A quantitative measure of the structural geometry, the Continuous Shape Measure (CSM) [24–26], is provided for each structure. Small CSM difference indicates high geometrical similarity. Each structure can have multiple CSM quantities with respect to multiple references. Only the minimum values are shown in this figure. Note that the CSM calculations omit the hydrogen atoms. The discrete spectral peaks are TDDFT simulation outputs.

2.1 Data preparation

2.1.1 Molecular dynamics simulations

Solvated Cu^{2+} ion was modeled using an ion in a cubic supercell with 48 water molecules at the experimental density of liquid water at ambient conditions. We carried out Car-Parrinello molecular dynamics simulations using the Quantum ESPRESSO package, [17] with interatomic forces derived from density functional theory (DFT) and the Perdew-Burke-Ernzerhof (PBE) exchange-correlation functional. [18] The interaction between valence electrons and ionic cores was represented by ultrasoft pseudopotentials; [19] we used a plane-wave basis set with energy cutoffs of 30 Ry and 300 Ry for the electronic wavefunction and charge density, respectively. All dynamics were run in the *NVT* ensemble at an elevated temperature of $T=380$ K to correct for the overstructuring of liquid water at ambient temperatures with the PBE functional. [20] A time step of 8 a.u. were employed with an effective mass of 500 a.u. with hydrogen substituted with deuterium. The water was first equilibrated for 10 ps before the Cu^{2+} ion was inserted into the system, after which the system was equilibrated for another 10 ps. This was followed by a 40 ps production run to extract the time-averaged properties of the system.

2.1.2 Optical absorption spectroscopy simulation

Time dependent density functional theory (TDDFT) [21] within the Tamm–Dancoff approximation [22] was used to obtain the optical excitation energies of the ion complexes. Specifically, 6846 aqua complexes were extracted roughly uniformly from the AIMD trajectory. Each complex consists of the copper ion and the surrounding water molecules within a radial cutoff of 2.92 \AA , which corresponds to the first minimum of the Cu-O partial radial distribution function for the Cu^{2+} oxidation state. All the optical calculations were carried out using the NWChem software package [23]. Here, an augmented cc-pVTZ basis was used for the copper ion while an augmented cc-pVDZ basis was used for the water molecules. Four examples of the aqua complexes and their corresponding TDDFT-calculated peaks in roughly the visible-infrared range are shown in Fig. 1. The aqua complexes data was partitioned into a training set of 6161 samples and a validation set of 685 samples.

2.1.3 High-throughput automation

To assist with the large number of copper complexes being studied, an AiiDA [27] workflow was employed to standardize and provide consistency for all calculations. AiiDA records full provenance between all calculations and ensures a robust framework for generating, storing, and analyzing results.

2.2 Data processing and analysis

2.2.1 Single-peak approximation

For GNN spectroscopy prediction, we focus on the TDDFT-calculated spectral peaks roughly in the visible-infrared range. Since the peak positions per structure tend to be close together, we approximated each cluster’s discrete peaks into a single unnormalized Gaussian curve (Fig. A.1). This approximation helps simplify the output format for training a structure-to-spectrum GNN model. For example, the original spectral peaks from TDDFT may be described by a set of tuples $(E_1, I_1), (E_2, I_2), \dots$, where E is the peak energy, and I is the peak intensity. After the approximation, we can simply describe the spectral signature with an unnormalized Gaussian, parametrized by the mean μ_G , the standard deviation σ_G , and the amplitude A_G . The single-peak approximation is further explained in the Appendices.

2.2.2 Shape analysis

We confirmed a geometry-spectroscopy correlation for the aqua complexes using a brief shape analysis based on Continuous Shape Measure, or CSM [24–26]. CSM describes deviation of a set of points (or atoms) relative to vertices of reference “ideal” polygons or polyhedra, and is typically applied to analyze the shapes of coordination complexes. Higher CSM value indicates more distortion or deviation from ideal shapes such as square, tetrahedron, sawhorse, pentagon, trigonal bipyramid, and so on. We calculated CSM values for the shapes formed by the central copper and the surrounding oxygens, for each aqua complex structure. As shown in Fig. B.1, an aqua complex’s shape information is clearly correlated with its spectral information. Further, as shown in Fig. 1ab, slight structural perturbations can result in noticeably different spectral outputs. Therefore, we conclude that the spectral signature is a geometry-sensitive property. More details regarding the shape analysis are described in the Appendices.

2.3 Graph representations

In the ALIGNN formulation [12], two types of graphs are used to encode an atomic structure: an original atomic graph \mathcal{G} and its corresponding line graph $\mathcal{L}(\mathcal{G})$. The nodes and edges in \mathcal{G} represent atoms and bonds, respectively. The nodes and edges in $\mathcal{L}(\mathcal{G})$, on the other hand, represent bonds and bond angles, respectively. Note that the edges in \mathcal{G} and the nodes in $\mathcal{L}(\mathcal{G})$ are identical entities and share the same embedding during GNN operation. In this work, we extended the ALIGNN encoding to also explicitly represent dihedral angles. This graph representation, or ALIGNN-d, is visualized in Fig. 2 for an arbitrary molecule in two different structural configurations. These two configurations cannot be distinguished with only the atom, bond (distance), and bond angle features; the additional information of the dihedral angle is necessary to establish two distinct graph encodings. Notably, the dihedral (torsion) angle, which ranges from 0° to 360° , can be used to resolve chirality for simple structures such as the one in Fig. 2. However, the application of ALIGNN-d for capturing enantiomers or learning chirality-dependent properties is outside the scope of this work. We hereby denote the line graph with the additional dihedral angle representation as $\mathcal{L}'(\mathcal{G})$.

We investigated the additional performance gain of using auxiliary line graphs by comparing GNN model accuracies based on different types of graph representations, with and without line graphs (Fig. 3). The minimally-connected graph \mathcal{G}_{\min} is meant to resemble typical molecular graph representations, which tend to require a minimal number of edges to connect the atoms together.

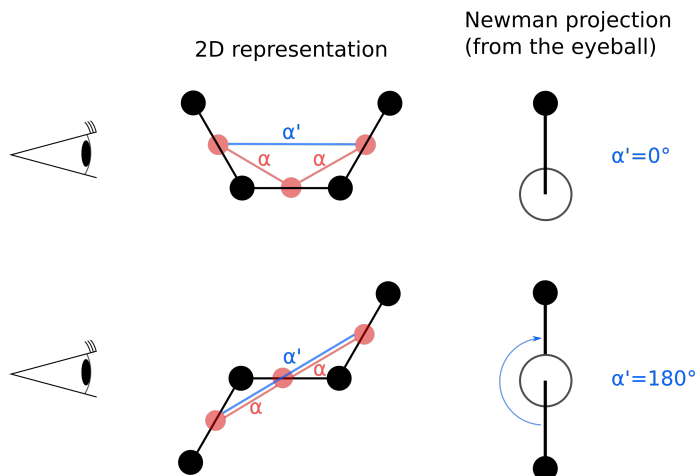


Figure 2: The line graphs, shown by colored nodes and edges, enable encoding angular information, which is absent in the original atomic graph (shown in black). In the line graphs, the red edges capture bond angles α , and the blue edges capture dihedral angles α' . A bond angle is simply the angle between any two adjacent bonds. A dihedral (torsion) angle is the clockwise angle in the Newman projection between any two bonds sharing a common bond.

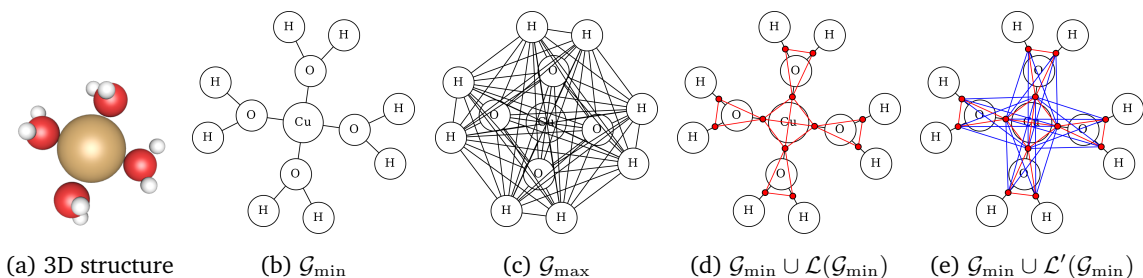


Figure 3: We investigated the expressive power of line graphs by comparing GNN model performances based on different graph representations of the solvated copper clusters, without (b,c) and with (d,e) line graphs. These graph representations (b-e) are shown for a 4-coordinated aqua complex (a) as an example.

Of all the graph representations studied in this work, \mathcal{G}_{\min} holds the least amount of information and thus is expected to result in the poorest performance, because bond angles and dihedral angles cannot be implicitly retrieved from \mathcal{G}_{\min} . The maximally-connected graph \mathcal{G}_{\max} , on the other hand, is a “brute-force” graph representation that encodes all pairwise bonds. Without considering line graphs, \mathcal{G}_{\max} in principle holds the fullest geometric information and thus is expected to result in high performance. Lastly, extending \mathcal{G}_{\min} by adding a corresponding line graph $\mathcal{L}(\mathcal{G}_{\min})$, or $\mathcal{L}'(\mathcal{G}_{\min})$, that captures bond angles, or both bond angles and dihedral angles, is expected to result in performance gain. The joint use of \mathcal{G} and $\mathcal{L}(\mathcal{G})$ is denoted by $\mathcal{G} \cup \mathcal{L}(\mathcal{G})$. We carried out model trainings based on these graph representations in order to determine the expressive power of $\mathcal{G}_{\min} \cup \mathcal{L}(\mathcal{G}_{\min})$ and $\mathcal{G}_{\min} \cup \mathcal{L}'(\mathcal{G}_{\min})$ relative to that of \mathcal{G}_{\min} and \mathcal{G}_{\max} .

In contrast to the original ALIGNN paper, we encoded the atomic, bond, and angular features with only the minimally required information, namely the atom type z , the bond distance d , the bond angle α , and the dihedral angle α' . In other words, in \mathcal{G} , each node corresponds to a value of z , and each edge corresponds to a value of d . In $\mathcal{L}(\mathcal{G})$, each node also corresponds to a value of d , and each edge corresponds to a value of α . Again, the edges in \mathcal{G} are identical to the nodes in $\mathcal{L}(\mathcal{G})$ and $\mathcal{L}'(\mathcal{G})$. Finally, in $\mathcal{L}'(\mathcal{G})$, each edge representing a dihedral angle corresponds to a value of α' . Information such as electronegativity, group number, bond type, and so on are not encoded.

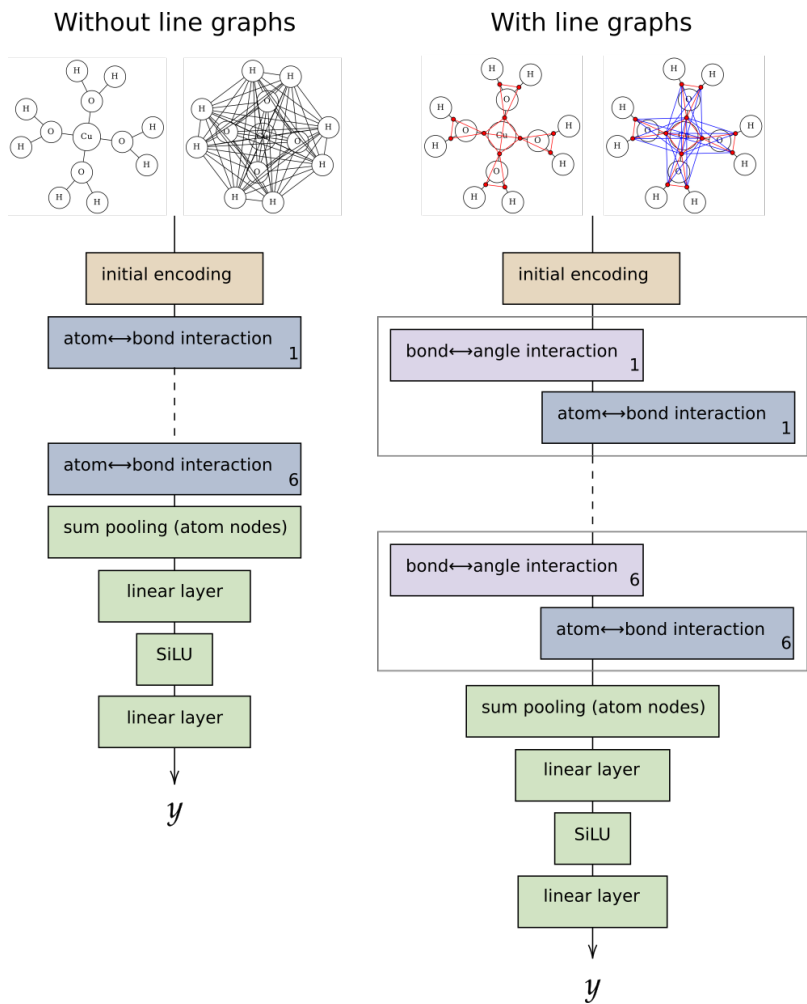


Figure 4: We kept the model architectures as identical as we could for evaluating and comparing GNN performances as a function of graph representations. For normal graphs, one graph convolution/interaction operation is defined. However, for graph representations with auxiliary line graphs, two interaction operations are necessary, where the atom-bond interaction operates on \mathcal{G} and the bond-angle interaction operates on $\mathcal{L}(\mathcal{G})$ or $\mathcal{L}'(\mathcal{G})$. Besides this difference, all other model parameters are the same (Table 1).

We used Atomic Simulation Environment [28] and PyTorch Geometric [29] to construct the graph representations, and to calculate bond and dihedral angles.

2.4 Model formulation

Two different GNN model architectures were defined: one for \mathcal{G}_{\min} and \mathcal{G}_{\max} ; and one for $\mathcal{G}_{\min} \cup \mathcal{L}(\mathcal{G}_{\min})$ and $\mathcal{G}_{\min} \cup \mathcal{L}'(\mathcal{G}_{\min})$. We kept the two architectures as identical as we could in order to fairly evaluate and compare the model performances as a function of input graph representation (Fig. 4). Both architectures consist of three parts: the initial encoding, the interaction operations, and the output layers.

In the initial encoding, the atom type, the bond distance, and the angular values are converted from scalars to feature vectors for subsequent neural network operations. The atom type z is transformed by an Embedding layer (see PyTorch documentation [30]). The bond distance d is expanded into a D -dimensional vector by the Radial Bessel basis functions, or RBF, proposed by

Klicpera *et al.* [11]. The n th element in the vector is expressed as

$$\text{RBF}_n(d) = \sqrt{\frac{2}{c}} \frac{\sin(\frac{n\pi}{c}d)}{d}, \quad (1)$$

where $n \in [1..D]$ and c is the cutoff value. We also used RBF to expand angular information. However, the angular encoding treats bond angles α and dihedral angles α' differently, and encodes their values at different channels of the expanded feature vector (Fig. C.1). Further details regarding the angular encoding are described in the Appendices.

The interaction operations are also known as the graph convolution/aggregation schemes. Following the ALIGNN paper [12], we also adopted the edge-gated graph convolution [31, 32] for the interaction operations. Notably, the edge-gated convolution updates both the nodes and the edges. The node features \mathbf{h}_i^{l+1} of node i at the $(l+1)$ th layer is updated as

$$\mathbf{h}_i^{l+1} = \mathbf{h}_i^l + \text{SiLU} \left(\text{LayerNorm} \left(\mathbf{W}_s^l + \sum_{j \in \mathcal{N}(i)} \hat{\mathbf{e}}_{ij}^l \odot \mathbf{W}_d^l \mathbf{h}_j^l \right) \right), \quad (2)$$

where SiLU is the Sigmoid Linear Unit activation function [33]; LayerNorm is the Layer Normalization operation [34]; \mathbf{W}_s and \mathbf{W}_d are weight matrices; the index j denotes the neighbor node of node i ; $\hat{\mathbf{e}}_{ij}$ is the edge gate vector for the edge from node i to node j ; and \odot denotes element-wise multiplication. The edge gate $\hat{\mathbf{e}}_{ij}^l$ at the l th layer is defined as

$$\hat{\mathbf{e}}_{ij}^l = \frac{\sigma(\mathbf{e}_{ij}^l)}{\sum_{j' \in \mathcal{N}(i)} \sigma(\mathbf{e}_{ij'}^l) + \epsilon}, \quad (3)$$

where σ is the sigmoid function, \mathbf{e}_{ij}^l is the original edge feature, and ϵ is a small constant for numerical stability. The edge features \mathbf{e}_{ij}^l is updated by

$$\mathbf{e}_{ij}^{l+1} = \mathbf{e}_{ij}^l + \text{SiLU} \left(\text{LayerNorm} \left(\mathbf{W}_g^l \mathbf{z}_{ij}^l \right) \right), \quad (4)$$

where \mathbf{W}_g is a weight matrix, and \mathbf{z}_{ij} is the concatenated vector from the node features \mathbf{h}_i , \mathbf{h}_j , and the edge features \mathbf{e}_{ij} :

$$\mathbf{z}_{ij} = \mathbf{h}_i \oplus \mathbf{h}_j \oplus \mathbf{e}_{ij}. \quad (5)$$

We applied the same edge-gated convolution scheme (Eq. 2–4) to operate on both the atomic graph \mathcal{G} and the line graphs $\mathcal{L}(\mathcal{G})$, $\mathcal{L}'(\mathcal{G})$. In the case of \mathcal{G} , the edge-gated convolution updates nodes that represent atoms, and edges that represent bonds, while exchanging information between the two, hence the term *atom-bond interaction*. In the case of $\mathcal{L}(\mathcal{G})$, the convolution updates nodes that represent bonds, and edges that represent angles, hence the term *bond-angle interaction*. Note that by iteratively applying the convolution operation on \mathcal{G} and $\mathcal{L}(\mathcal{G})$, the angular information stored in $\mathcal{L}(\mathcal{G})$ can propagate to \mathcal{G} . Due to the nature of the edge-gated convolution, all the feature/embedding vectors for atoms, bonds, and angles during the interaction layers have the same length, or the same number of channels D .

Lastly, the final output layers pool (by summation) the node features of \mathcal{G} and transform the pooled embedding into an output vector \mathbf{y} , which, in this work, is a three-dimensional vector consisted of the parameters of an unnormalized Gaussian curve μ_G , σ_G , and A_G . The two Linear layers have the output lengths of 64 and 3, respectively.

2.5 Model training

We used PyTorch Geometric [29] to develop the GNN models. Note that although two model architectures were defined, a total of four GNN models were trained due to the four different graph representations studied in this work. Nonetheless, these models have the same parameters (Table 1). Similar to the ALIGNN paper [12], we trained each model using the Adam optimizer

Table 1: Model parameters

Name	Notation	Value
Number of interaction layers	L	6
RBF cutoff (bond distance)	c_d	6.0 Å
RBF cutoff (cosine and sine angles)	c_α	2.0
Number of channels	D	64

Table 2: Training parameters

Name	Notation	Value
Batch size	M	128
Number of epochs	N_{ep}	1000
Initial learning rate	η_{init}	0.0001
Maximum learning rate (1cycle)	η_{max}	0.001
First moment coefficient for Adam	β_1	0.9
Second moment coefficient for Adam	β_2	0.999

[35] and the 1cycle scheduler [36]. Each training was carried out in PyTorch [30] and PyTorch Geometric [29] on a NVIDIA V100 (Volta) GPU, and repeated eight times with randomly initialized weights for statistical robustness. The mean squared error (MSE) was used as the loss during training. The training parameters are the same for each training (Table 2). All other parameters, if unspecified in this work, default to values per PyTorch 1.8.1 and PyTorch Geometric 1.7.2.

3 Results and discussion

We first briefly discuss the memory efficiency of using auxiliary line graphs. The number of edges in each graph representation studied in this work is listed in Table 3. Although constructing line graphs on top of \mathcal{G}_{min} introduces additional edges, the total amount of edges does not exceed that of \mathcal{G}_{max} . Notably, $\mathcal{G}_{\text{min}} \cup \mathcal{L}'(\mathcal{G}_{\text{min}})$ has roughly 31–35% fewer edges relative to \mathcal{G}_{max} , but its expressive power, as will be discussed later, is roughly the same. In other words, $\mathcal{G}_{\text{min}} \cup \mathcal{L}'(\mathcal{G}_{\text{min}})$ leads to roughly the same model accuracy as that of \mathcal{G}_{max} , but with significantly fewer edges. Note that line graphs do not technically introduce additional nodes, since the nodes of $\mathcal{L}(\mathcal{G})$ are identical to the edges of \mathcal{G} and therefore requires minimal additional memory. Aside from memory, the computational cost of using auxiliary line graphs is harder to determine. In the original ALIGNN formulation and also in this work, each interaction layer consists of two graph convolutions, one over \mathcal{G} and one over $\mathcal{L}(\mathcal{G})$. Therefore, using line graphs introduces additional computations. Future work is necessary to more thoroughly determinate the compound cost of smaller memory requirement and higher computational overhead.

We observed several important findings based on the validation losses during the model training (Fig. 5). First, as expected, using auxiliary line graphs $\mathcal{L}(\mathcal{G})$ and $\mathcal{L}'(\mathcal{G})$ led to significant performance improvement over the minimum baseline \mathcal{G}_{min} , which in fact appears to lead to overfitting. Second, including the additional dihedral angle encoding, i.e., $\mathcal{L}'(\mathcal{G}_{\text{min}})$, over $\mathcal{L}(\mathcal{G}_{\text{min}})$ led to noticeably better performance. This improvement is important, because without the dihedral angles, the per-

Table 3: Number of edges in each graph representation based on the aqua complexes, which are copper ions coordinated by 4, 5, or 6 water molecules.

	\mathcal{G}_{min}	$\mathcal{G}_{\text{min}} \cup \mathcal{L}(\mathcal{G}_{\text{min}})$	$\mathcal{G}_{\text{min}} \cup \mathcal{L}'(\mathcal{G}_{\text{min}})$	\mathcal{G}_{max}
4-coordinated	12	30	54	78
5-coordinated	15	40	80	120
6-coordinated	18	51	111	171

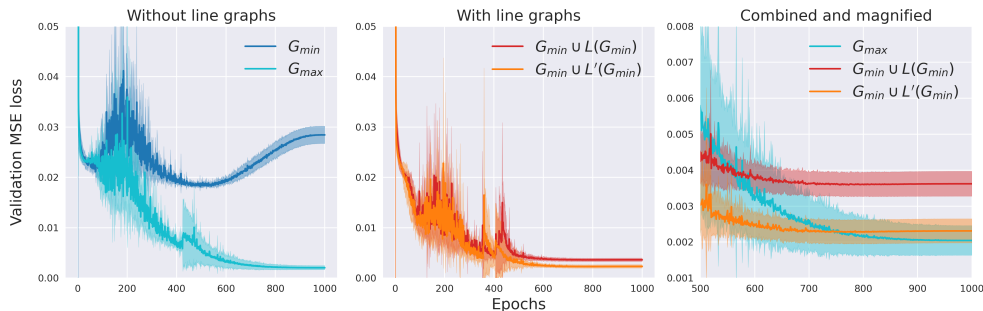


Figure 5: The validation losses during training for the four graph representations studied in this work: \mathcal{G}_{\min} , \mathcal{G}_{\max} , $\mathcal{G}_{\min} \cup \mathcal{L}(\mathcal{G}_{\min})$, and $\mathcal{G}_{\min} \cup \mathcal{L}'(\mathcal{G}_{\min})$. Each training was repeated eight times, the standard deviations of which are shown by the semi-transparent regions. The averages of the repeats are shown by the solid lines. The large loss fluctuations are attributed to the 1cycle scheduler, which increases learning rate during early training.

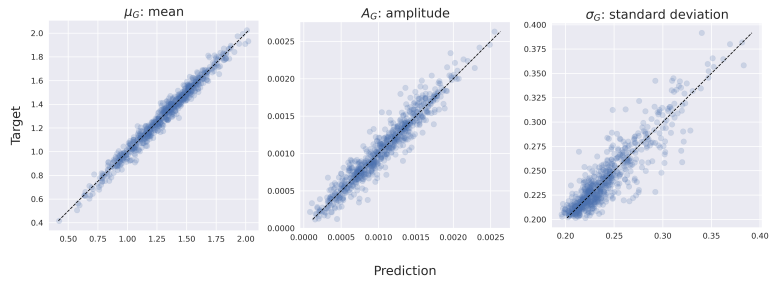
formance based on $\mathcal{G}_{\min} \cup \mathcal{L}(\mathcal{G}_{\min})$ cannot reach to that of the maximally-connected graph \mathcal{G}_{\max} . Third, the losses based on representations with auxiliary line graphs converge faster (with respect to the number of epochs) and are more stable than those without line graphs. Lastly, the final performance based on $\mathcal{G}_{\min} \cup \mathcal{L}'(\mathcal{G}_{\min})$, which is the proposed ALIGNN-d encoding in this work, is about the same as that of \mathcal{G}_{\max} .

As suggested by these findings, the expressive power of using auxiliary line graphs, with dihedral angles, is roughly the same as that of the far less scalable maximally-connected graph. Note that the $\mathcal{G}_{\min} \cup \mathcal{L}(\mathcal{G}_{\min})$ representation, with only bond angle information, is not guaranteed to capture all structural details (as proven in Fig. 2); this statement is also supported by the performance gap between $\mathcal{G}_{\min} \cup \mathcal{L}(\mathcal{G}_{\min})$ and \mathcal{G}_{\max} shown in Fig.5. Therefore, the additional dihedral encoding is necessary to capture full structural information. Since \mathcal{G}_{\max} is computationally intractable for large-scale systems, we propose the ALIGNN-d encoding as an alternative, memory-efficient graph representation while maintaining the same level of expressive power. Also, explicitly encoding angular information appears to facilitate a faster and more stable learning, with less fluctuations in the losses during training.

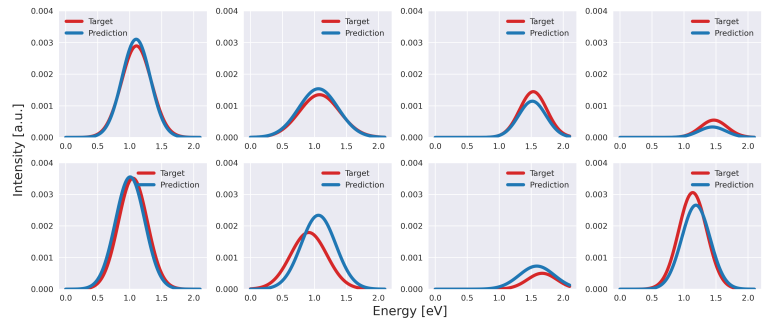
We validated ALIGNN-d by examining the validation accuracy for one of the trained models based on $\mathcal{G}_{\min} \cup \mathcal{L}'(\mathcal{G}_{\min})$, as shown in Fig. 6. The validation predictions are accurate for the Gaussian mean μ_G and amplitude A_G , and reasonably accurate for the standard deviation σ_G . Further, when plotted in the form of Gaussian curves, the validation predictions are reasonably accurate, with some minor deviations from the target curves.

Lastly, we explored model interpretability for ALIGNN-d. Specifically, we designed a certain model architecture such that the output is the sum of all graph components. In other words, the atoms, bonds, and angles—which are explicitly represented in graph encoding—all contribute to the final model output. This model architecture is the same as the model with line graph encoding shown in Fig.4, except for the final output layers. In this specific architecture, after the interaction layers, all the embedding vectors were transformed into scalars by a Linear layer, followed by the Softplus activation function $\ln(1 + e^x)$, which gives a non-negative value. These non-negative scalars corresponding to atoms, bonds, and angles are then summed to give the model output.

We trained such an “interpretable” variant of ALIGNN-d to predict spectral peak intensity, a positive quantity. Therefore, the model can be interpreted such that each of the graph components—the atoms, the bonds, and the angles—holds a non-negative scalar that contributes to the Gaussian peak intensity A_G . These contributions can be visualized in the graph format, indicating components of significant contributions (Fig. 7). Based on the example shown in Fig. 7, the peak intensity is primarily attributed to the central copper atom and most O-Cu-O bonds, followed by certain dihedral angles and Cu-O bonds. Most other components have essentially zero contribution to peak intensity, as indicated by the logarithmic scale of the colorbar.



(a) Parity plots



(b) 8 randomly sampled predicted peaks vs. target peaks

Figure 6: The validation predictions based on $\mathcal{G}_{\min} \cup \mathcal{L}'(\mathcal{G}_{\min})$, or the ALIGNN-d encoding, are reasonably accurate. To demonstrate this, the predicted and the target Gaussian peaks (parametrized by μ_G , A_G , and σ_G) for one of the trained models based on $\mathcal{G}_{\min} \cup \mathcal{L}'(\mathcal{G}_{\min})$ are shown in parity plots (a). Additionally, 8 randomly sampled peak predictions, in the form of the Gaussian curve, are plotted against the validation targets (b).

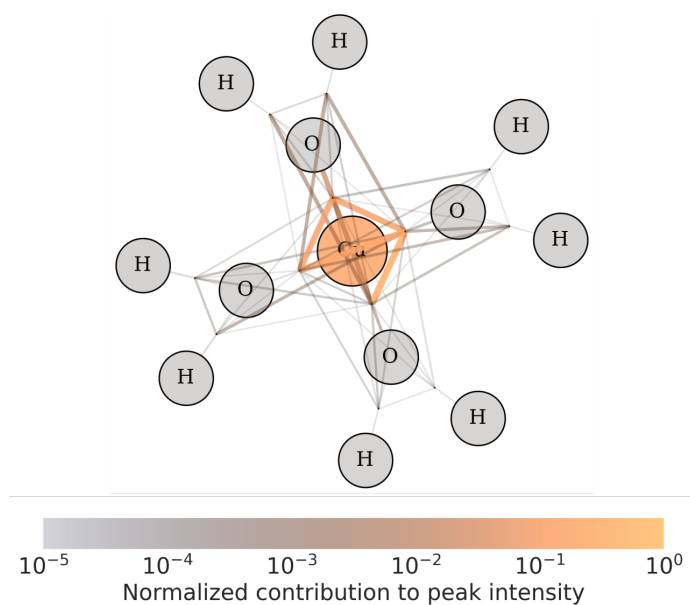


Figure 7: Explicit representation of bond and dihedral angles enables a unique approach to GNN model interpretability, allowing the contributions of the atomic, bond, and angular components to the model output to be visualized in an intuitive graph format. Based on the example shown here, the spectral peak intensity A_G is primarily attributed to the central copper and most O-Cu-O bond angles, followed by certain dihedral angles and Cu-O bonds. The magnitudes of the relative contributions are colored according to the colorbar. Also, for the angle components (the edges in the line graph), larger edge thickness indicates higher contribution. Most components have essentially zero contribution to peak intensity, as indicated by the logarithmic scale of the colorbar.

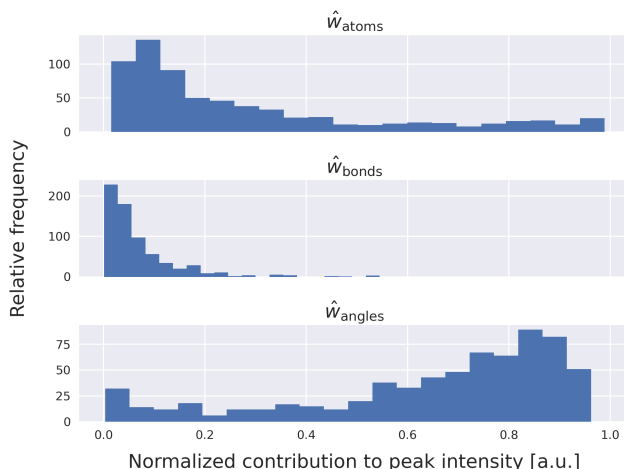


Figure 8: Based on the “interpretable” variant of ALIGNN-d, the predicted peak intensity is often attributed to the angular components, followed by the atom components. The bond components in general have the smallest contribution. These contributions are based on the validation dataset.

However, such an interpretable visualization is still dense, and it can be cumbersome to clearly distinguish the individual graph components for all other structures in the dataset. Therefore, we performed a simplified analysis where the model output, i.e., the peak intensity, is partitioned into three main contributions: the sum of atomic components w_{atoms} , the sum of bond components w_{bonds} , and the sum of angular components w_{angles} . In other words, each aqua complex structure corresponds to a set of these three numbers $(w_{atoms}, w_{bonds}, w_{angles})$. Based on the histograms of these contributions, the angles often contribute significantly to the model output, more than the atoms and bonds. This finding agrees to our intuition that the angular information is critical for informing spectroscopy. It also supports the merit of explicitly representing or encoding structural features beyond just atoms and bonds (e.g., bond and dihedral angles) in the graph representation.

4 Conclusions

As shown in this work, the auxiliary line graph encoding, which explicitly represents bond and dihedral angles, is suitable for training GNNs to predict geometry-sensitive spectroscopy of aqua copper complexes. Based on the results, extending the line graph encoding originally developed by DeCost and Choudhary [12], or ALIGNN, to also explicitly represent dihedral angles led to higher GNN model accuracy. Additionally, the model accuracy based on such encoding, or ALIGNN-d, is roughly the same as that based on the “brute-force”, maximally-connected graph \mathcal{G}_{max} , which encodes all pairwise interatomic bonds. This finding suggests a memory-efficient, principled approach to graph encoding, where the combination of a minimally-connected graph \mathcal{G}_{min} and its corresponding line graph with dihedral angles $\mathcal{L}'(\mathcal{G}_{min})$ can replace the far less scalable maximally-connected \mathcal{G}_{max} with significantly fewer edges.

We also briefly explored model interpretability for ALIGNN-d by considering the model output as a sum of all graph components, and the relative contributions from the components were visualized in an intuitive graph format. Based on a simple analysis of the contributions, the angles are shown to be important to spectroscopy prediction of the aqua copper complexes, more often than the atoms and bonds. This exploratory research on model interpretability for GNNs with auxiliary line graphs also sheds light on the merit of using a more elaborate, *layered* graph representation to better capture the structural information of atomic systems.

As previously stated, the idea of encoding angles with line graphs is a general method for various different atomic graphs. While the original ALIGNN paper [12] focuses on general material property prediction for periodic, crystalline systems and small-scale molecules, our work focuses on disordered and distorted systems, and a geometry-sensitive property that arises from structural perturbations. Therefore, in conclusion, ALIGNN-d is a general, memory-efficient graph encoding method capable of capturing the full structural information of a wide range of atomic systems, including ordered and disordered, periodic and non-periodic structures.

However, aside from memory efficiency, the use of auxiliary line graphs introduces additional computations. Future work is therefore necessary to more thoroughly determine the computational cost and scalability of ALIGNN and ALIGNN-d. Also, we acknowledge that in contrast to paiNN [13], ALIGNN-d does not incorporate directional information, and therefore cannot be used to predict tensorial properties, or direction-specific properties. While ALIGNN-d's lack of directional encoding may be considered as a relative disadvantage, ALIGNN-d and paiNN are not necessarily mutually exclusive formulations, and future work may involve combining angular encoding (with line graphs) and equivariant directional encoding. Lastly, we have only begun to explore model interpretability for GNNs with auxiliary line graphs. Not all physical properties are manifested as a simple summation of atomic, bond, or angular components, as formulated in this work. Therefore, a more elaborate interpretation method is necessary to further elucidate how a physical property may arise with respect to the structural or chemical features of an atomic system. Such research is essential for explainable machine learning in scientific applications.

Data Availability

All data required to reproduce this work can be requested by contacting the corresponding author.

Acknowledgements

The authors are partially supported by the Laboratory Directed Research and Development (LDRD) program (20-SI-004) at Lawrence Livermore National Laboratory. This work was performed under the auspices of the US Department of Energy by Lawrence Livermore National Laboratory under contract No. DE-AC52-07NA27344.

Conflict of Interest

On behalf of all authors, the corresponding author states that there is no conflict of interest.

References

1. Gilmer, J., Schoenholz, S. S., Riley, P. F., Vinyals, O. & Dahl, G. E. *Neural message passing for quantum chemistry* in *International conference on machine learning* (2017), 1263–1272.
2. Coley, C. W., Barzilay, R., Green, W. H., Jaakkola, T. S. & Jensen, K. F. Convolutional embedding of attributed molecular graphs for physical property prediction. *Journal of chemical information and modeling* **57**, 1757–1772 (2017).
3. Schütt, K. T., Sauceda, H. E., Kindermans, P.-J., Tkatchenko, A. & Müller, K.-R. SchNet—a deep learning architecture for molecules and materials. *The Journal of Chemical Physics* **148**, 241722 (2018).
4. Xie, T. & Grossman, J. C. Crystal graph convolutional neural networks for an accurate and interpretable prediction of material properties. *Physical review letters* **120**, 145301 (2018).
5. Yang, K. *et al.* Analyzing learned molecular representations for property prediction. *Journal of chemical information and modeling* **59**, 3370–3388 (2019).

6. Chen, C., Ye, W., Zuo, Y., Zheng, C. & Ong, S. P. Graph networks as a universal machine learning framework for molecules and crystals. *Chemistry of Materials* **31**, 3564–3572 (2019).
7. Linker, G.-J., van Duijnen, P. T. & Broer, R. Understanding Trends in Molecular Bond Angles. *The Journal of Physical Chemistry A* **124**, 1306–1311 (2020).
8. Timoshenko, J. & Frenkel, A. I. “Inverting” X-ray absorption spectra of catalysts by machine learning in search for activity descriptors. *Acs Catalysis* **9**, 10192–10211 (2019).
9. Guda, A. *et al.* Machine learning approaches to XANES spectra for quantitative 3D structural determination: The case of CO₂ adsorption on CPO-27-Ni MOF. *Radiation Physics and Chemistry* **175**, 108430 (2020).
10. Guda, A. A. *et al.* Quantitative structural determination of active sites from in situ and operando XANES spectra: from standard ab initio simulations to chemometric and machine learning approaches. *Catalysis Today* **336**, 3–21 (2019).
11. Klicpera, J., Groß, J. & Günnemann, S. Directional message passing for molecular graphs. *arXiv preprint arXiv:2003.03123* (2020).
12. DeCost, B. & Choudhary, K. Atomistic Line Graph Neural Network for Improved Materials Property Predictions. *arXiv preprint arXiv:2106.01829* (2021).
13. Schütt, K. T., Unke, O. T. & Gastegger, M. Equivariant message passing for the prediction of tensorial properties and molecular spectra. *arXiv preprint arXiv:2102.03150* (2021).
14. Chapman, J., Batra, R. & Ramprasad, R. Machine learning models for the prediction of energy, forces, and stresses for Platinum. *Computational Materials Science* **174**, 109483 (2020).
15. Chapman, J., Goldman, N. & Wood, B. A Physically-informed Graph-based Order Parameter for the Universal Characterization of Atomic Structures. *arXiv preprint arXiv:2106.08215* (2021).
16. Parsons, J., Holmes, J. B., Rojas, J. M., Tsai, J. & Strauss, C. E. Practical conversion from torsion space to Cartesian space for in silico protein synthesis. *Journal of computational chemistry* **26**, 1063–1068 (2005).
17. Giannozzi, P. *et al.* QUANTUM ESPRESSO: a modular and open-source software project for quantum simulations of materials. *Journal of physics: Condensed matter* **21**, 395502 (2009).
18. Perdew, J. P., Burke, K. & Ernzerhof, M. Generalized gradient approximation made simple. *Physical review letters* **77**, 3865 (1996).
19. Vanderbilt, D. Soft self-consistent pseudopotentials in a generalized eigenvalue formalism. *Physical review B* **41**, 7892 (1990).
20. Grossman, J. C., Schwegler, E., Draeger, E. W., Gygi, F. & Galli, G. Towards an assessment of the accuracy of density functional theory for first principles simulations of water. *The Journal of chemical physics* **120**, 300–311 (2004).
21. Runge, E. & Gross, E. K. Density-functional theory for time-dependent systems. *Physical Review Letters* **52**, 997 (1984).
22. Hirata, S. & Head-Gordon, M. Time-dependent density functional theory within the Tamm-Dancoff approximation. *Chemical Physics Letters* **314**, 291–299 (1999).
23. Apra, E. *et al.* NWChem: Past, present, and future. *The Journal of chemical physics* **152**, 184102 (2020).
24. Pinsky, M. & Avnir, D. Continuous symmetry measures. 5. The classical polyhedra. *Inorganic chemistry* **37**, 5575–5582 (1998).
25. Casanova, D. *et al.* Minimal distortion pathways in polyhedral rearrangements. *Journal of the American Chemical Society* **126**, 1755–1763 (2004).
26. Cirera, J., Ruiz, E. & Alvarez, S. Shape and Spin State in Four-Coordinate Transition-Metal Complexes: The Case of the d₆ Configuration. *Chemistry—A European Journal* **12**, 3162–3167 (2006).

27. Huber, S. P. *et al.* AiiDA 1.0, a scalable computational infrastructure for automated reproducible workflows and data provenance. *Scientific data* **7**, 1–18 (2020).
28. Larsen, A. H. *et al.* The atomic simulation environment—a Python library for working with atoms. *Journal of Physics: Condensed Matter* **29**, 273002 (2017).
29. Fey, M. & Lenssen, J. E. Fast graph representation learning with PyTorch Geometric. *arXiv preprint arXiv:1903.02428* (2019).
30. Paszke, A. *et al.* Pytorch: An imperative style, high-performance deep learning library. *Advances in neural information processing systems* **32**, 8026–8037 (2019).
31. Bresson, X. & Laurent, T. Residual gated graph convnets. *arXiv preprint arXiv:1711.07553* (2017).
32. Dwivedi, V. P., Joshi, C. K., Laurent, T., Bengio, Y. & Bresson, X. Benchmarking graph neural networks. *arXiv preprint arXiv:2003.00982* (2020).
33. Elfving, S., Uchibe, E. & Doya, K. Sigmoid-weighted linear units for neural network function approximation in reinforcement learning. *Neural Networks* **107**, 3–11 (2018).
34. Ba, J. L., Kiros, J. R. & Hinton, G. E. Layer normalization. *arXiv preprint arXiv:1607.06450* (2016).
35. Kingma, D. P. & Ba, J. Adam: A method for stochastic optimization. *arXiv preprint arXiv:1412.6980* (2014).
36. Smith, L. N. & Topin, N. *Super-convergence: Very fast training of neural networks using large learning rates in Artificial Intelligence and Machine Learning for Multi-Domain Operations Applications* **11006** (2019), 1100612.
37. Virtanen, P. *et al.* SciPy 1.0: Fundamental Algorithms for Scientific Computing in Python. *Nature Methods* **17**, 261–272 (2020).

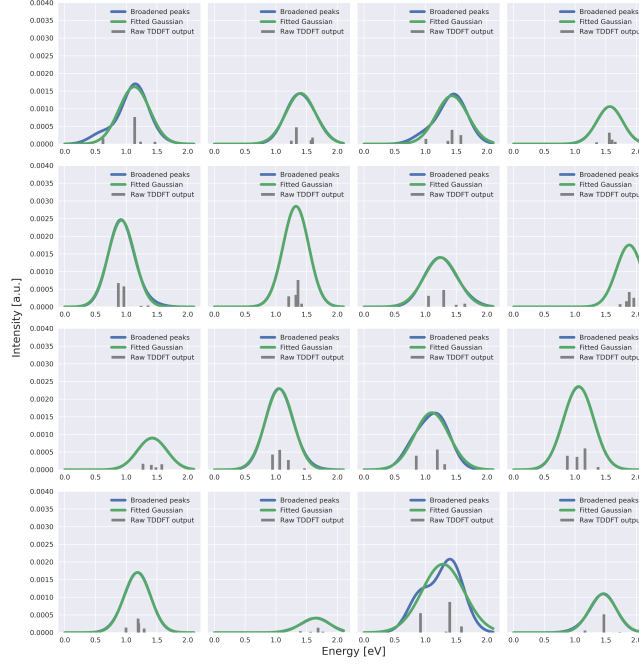


Figure A.1: The TDDFT-calculated discrete spectral peaks (vertical, gray lines) in roughly the visible-infrared range tend to be close together and were approximated to be a single Gaussian curve. The approximation is based on first broadening the discrete peaks with a Gaussian kernel and then fitting the broadened peaks (blue curves) with a Gaussian function (green curves). 16 randomly sampled spectral signatures and their corresponding approximations are shown.

Appendix A Single-peak approximation

The single-peak approximation of the discrete spectral lines is based on peak broadening, followed by a simple least-square fitting of a single unnormalized Gaussian curve. The broadening step is equivalent to kernel density estimation

$$\hat{f}(x) = \sum_{i=1}^N K(x - x_i), \quad (6)$$

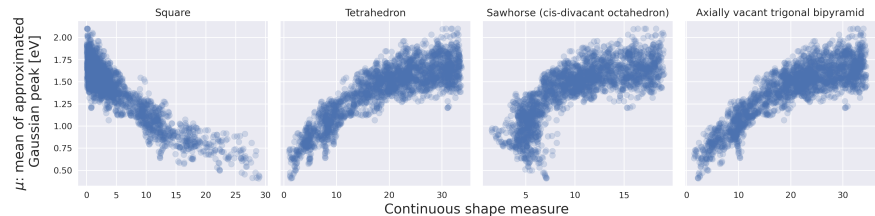
where $\hat{f}(x)$ is the broadened function or spectrum over the energy values x , N is the number of discrete peaks, and K is the kernel function. We used a Gaussian kernel with a standard deviation of 0.2 eV. The least-square fitting was implemented using SciPy [37]. The fitted Gaussian curve

$$g(x) = A_G \frac{1}{\sigma_G \sqrt{2\pi}} \exp \frac{-1}{2} \left(\frac{x - \mu_G}{\sigma_G} \right)^2 \quad (7)$$

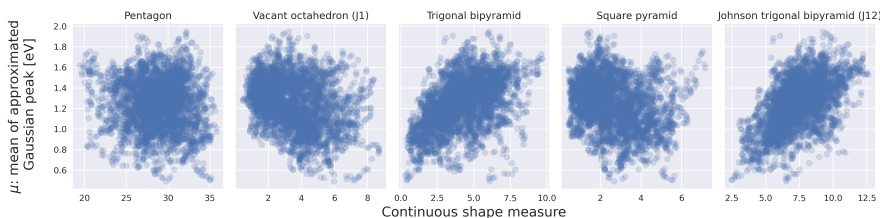
is parametrized by the mean μ_G , the standard deviation σ_G , and the amplitude A_G .

Appendix B Shape analysis

We calculated the CSM [24–26] for the shapes formed by the central copper atom and the coordinated oxygen atoms from the copper cluster data. In the case of 4 oxygens surrounding the copper atom, the ideal reference shapes are square, tetrahedron, sawhorse, and axially vacant trigonal bipyramid. In the case of 5 oxygens, the ideal reference shapes are pentagon, vacant octahedron



(a) 4 oxygens in each cluster



(b) 5 oxygens in each cluster

Figure B.1: A solvated copper cluster’s shape information is correlated with its spectral information, as shown in these scatter plots, where each scatter point represents a cluster structure. The shape quantity (y-axis) is continuous shape measure (CSM), a measure of deviation from an ideal reference polyhedron (indicated by subplot title), whereas the spectral quantity (x-axis) is the mean of the fitted Gaussian peak (see Fig. A.1). This shape-spectrum correlation is especially strong for clusters containing 4 oxygens or water molecules (a), but less so for clusters containing 5 oxygens (b). Nonetheless, in (b), there is some observable correlation between two CSM quantities (trigonal bipyramid and Johnson trigonal bipyramid) and the spectral quantity.

(or the J_1 Johnson solid), trigonal bipyramid, square pyramid, and the Johnson trigonal bipyramid (J_{12}). For each reference shape, the CSM is plotted against the mean of the approximated Gaussian peak μ , as shown in Fig. B.1. Significant correlation between CSM and μ can be clearly observed with respect to certain reference shapes. This result suggests that the spectral signature of the solvated copper clusters is a geometry-sensitive property. Note that the CSM quantities here do not account for the hydrogen atoms in the clusters. Also, clusters containing 6 oxygens are rare and thus were omitted.

Appendix C Angular encoding

The angular encoding treats bond angles α and dihedral angles α' as two different types of angles, and encodes their values at different channels of the expanded feature vectors \mathbf{e} , which correspond to the edges of line graphs. The bond angle is encoded in the first half of \mathbf{e} , and the dihedral angle is encoded in the second half. While the bond angle ranges from 0° to 180° , the dihedral (torsion) angle ranges from 0° to 360° . The use of trigonometric functions (sine and cosine) informs the model the periodic nature of the dihedral angle, i.e., there is little physical difference between 1° and 359° . It is also necessary to use both sine and cosine functions to retain the full dihedral angle information. Therefore, the encoding of the dihedral angle is further divided into the cosine and sine components, each occupying a quarter of the channels of the feature vector. The unoccupied parts of the feature vector are initialized with zeros. Lastly, since the sine and cosine values range from -1 to 1, these values are added by 1 prior to the RBF expansion (Eq. 1) with a cutoff value of $c = 2$.

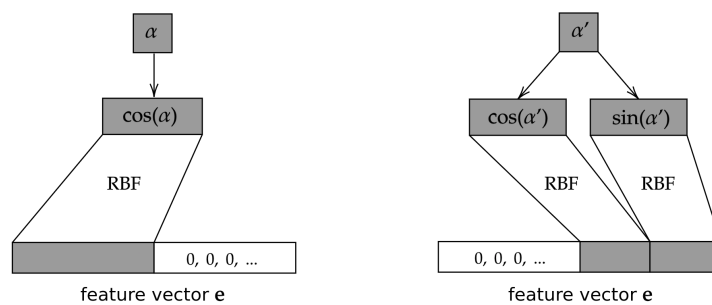


Figure C.1: Angular encoding for bond angles α and dihedral angles α' . The angular values, in the form of sine and cosine functions, are expanded into feature vectors by RBF (Eq. 1).